Computational Particle Mechanics
https://doi.org/10.1007/s40571-020-00358-x

Particle-scale numerical modeling of thermo-mechanical phenomena for additive manufacturing using the material point method

Takashi Maeshima[1] · **Youngkyu Kim**[1] · **Tarek I. Zohdi**[1]

Received: 30 March 2020 / Revised: 20 August 2020 / Accepted: 3 September 2020

Abstract
A fundamental numerical model at the powder particle scale based on the material point method (MPM) is developed for selective laser sintering (SLS). In order to describe the thermo-mechanical phenomena, a laser heat source model with a Gaussian energy distribution and the Perzyna viscoplastic model with a return mapping algorithm are employed. The principal process conditions, such as the laser power and radius, and the scanning speed are systematically varied. Based on the obtained temperature distribution generated by laser irradiation under these conditions, elastic–viscoplastic stresses were calculated to evaluate the deformation of powder particle pairs under the driving force of surface tension via a simple two-dimensional test case. The developed MPM model can capture minute changes of the deformation behavior and the temperature distribution history during melting and consolidation at the particle scale. Melting and consolidation of particle pairs during SLS are basic nature in determining the final product quality. The model can help to evaluate variations in the fusion of microscopic areas, melted by a laser, resulting from variations in the process conditions.

Keywords Material point method · Particle-scale modeling · Additive manufacturing · Viscoelasto-plastic model

1 Introduction

Selective laser sintering (SLS) and selective laser melting (SLM) are laser fusion additive manufacturing (AM) processes that have attracted attention in recent years due to the ability to achieve high design flexibility to create unprecedented components. These processes are layer-by-layer processes, in which the laser selectively melts the powder layer in accordance with two-dimensional (2D) slice data generated from three-dimensional (3D) computer-aided design models. Accurate melting of the predetermined microscopic region at the powder particle scale will create high-quality AM parts. To control the melting in such microscopic regions, the optimal powder characteristics and process input parameters need to be determined, which requires expensive and time-consuming trial-and-error experimental approaches. An attractive alternative to answering this challenge is through a numerical modeling approach. Numerical models can help manufacturers achieve a better prediction on the behavior of a powder melting process to control a microscopic region and determine powder specification and process parameters. Several works have been done to model the metallic powder melting process in mesh-based numerical approach such as Eulerian finite-element [20], finite-volume [35] and finite-difference methods [4]. While these mesh-based numerical methods are capable of producing high-fidelity solutions and have been adapted to laser fusion additive manufacturing, the process causes an evolution of the free surface and large deformations, which are difficult to represent with the aforementioned methods. Meshfree methods are proposed to model such intrinsic topological requirements for laser fusion additive manufacturing process. Ganeriwala and Zohdi [17] developed a discrete-element method framework to simulate a single laser track on SLS process. Wessels et al. [34] modeled a thermo-mechanical phase change to evaluate powder melting and consolidation using optical transportation meshfree method. Russell et al. [26] simulated melt pool dynamics on the powder scale by smoothed particle hydrody-

T. Maeshima and Y. Kim authors are contributed equally to this work.

✉ Takashi Maeshima
t_maeshima@berkeley.edu

Youngkyu Kim
youngkyu_kim@berkeley.edu

Tarek I. Zohdi
zohdi@berkeley.edu

[1] University of California, Berkeley, Etcheverry Hall, Berkeley, CA 94720-1740, USA

Published online: 15 September 2020

namics (SPH) approach. Fürstenau et al. [16] have presented an efficient parallelization using SPH on graphics processing unit (GPU) for the large-scale realistic 3D melt track of SLM process. Laser fusion additive manufacturing is not restricted to metallic powders, however, as it also applies to polymeric powders [21,22]. Thus, the numerical simulations have been developed to predict for SLS process. Balemans et al. [6] model the laser sintering of a pair polymeric powder in 2D to study the sintering behavior in mesh-based numerical approach, while Bierwisch et al. [8] developed melt track simulations on powder scale using meshfree SPH approach.

The material point method (MPM) combines Lagrangian material points with Eulerian Cartesian grids proposed by Sulsky et al. [30]. The continuum domain is represented with a set of material points, and all state variables and the kinematic variables are stored at material points (Fig. 1). Material points flow through a fixed background grid within each time step during the simulation. The stored data are mapped onto the background grid using interpolation functions and updated with the governing equations. Then, the data are remapped to the material points from the background grid. MPM has been used in the solid mechanics field because of its advantages. The MPM can handle large deformations, and it makes use of various constitutive laws with ease since Lagrangian particles allow easy implementation of constitutive models [7,31]. Thus, the MPM may be a good way to analyze the interaction during a phase change (e.g., solid to liquid, and vice versa). Indeed, there have been reports of extending this method to fluid mechanics with solid–liquid interactions. Stomakhin et al. [29] introduced an MPM framework with an elasto-plastic constitutive relation to simulate melting and solidification in animations. Yang et al. [36] presented solid–fluid (water) interactions problems using MPM with a flux-based algorithm. However, there is no report that MPM has been applied to the laser fusion AM processes. Although computational efficiency is a critical issue for MPM to simulate problems such as large-scale laser fusion AM processes, the MPM offers the potential for a massively parallelized approach presented by Dong and Grabe [12] and Wang et al. [33]. Once the basic framework of MPM for laser fusion AM is established, it will be a promising application to predict large-scale laser fusion AM process by the parallelization approach.

In this study, we focus on SLS process and constructed a framework for solving thermo-mechanical phenomena to consider laser melting behavior of the powder scale using MPM. Since the diameter of feed powder particles is micrometer size in laser melting processes, the influence of surface–volume ratio is large. Thus, it is necessary to consider the surface tension in the laser melting process. In contrast, due to high molecular weight there is no evaporation in the case of polymeric powder fusion, unlike in the case of metallic powder fusion, and thus, the evaporation does not take into account to this work. Typical polymers used in SLS process are semicrystalline polymer such as polyamide 6 (PA6) and polyamide 12 (PA12), e.g., the crystallinity of PA12 is about 25% in SLS parts [23]. The feed materials are pre-heated to nearly crystallized temperature, T_c, in the deposited state. Then, the feed materials are heated by laser irradiation above the melting point, T_m, to be consolidated [25]. Below glass transition temperature, T_g, the semicrystalline polymers exhibit viscoplastic behavior under large deformation, while they exhibit viscoelastic behavior with small strain [3,19]. Above T_g, it has been reported to have both viscoelastic and viscoplastic behaviors depending on the ratio of crystallinity [1,13]. As described above, SLS process starts near T_c and the temperature rapidly increases above T_m in the process. A constitutive model is thus considered viscoelasto-plastic deformation since semicrystalline polymer with low crystallinity is assumed to be viscoplastic material during laser melting process. Therefore, the proposed framework implements the surface tension effect and viscoelasto-plastic model. Details of the surface tension and constitutive models will be presented in Sect. 2.

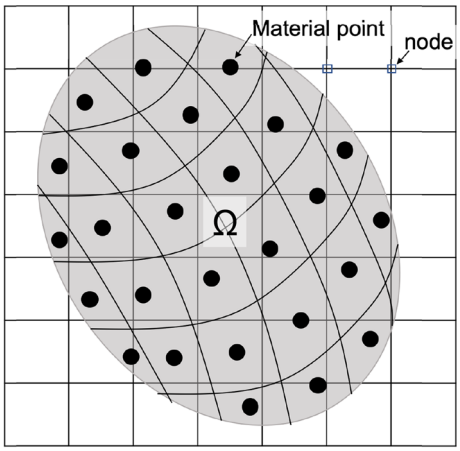

Fig. 1 Lagrangian material points overlaid over an Eulerian grid

2 Background theory

The primary purpose of presenting this section here is to introduce the governing equations and formulations used for mechanical and thermal fields coupled with a surface tension and a viscoelasto-plastic model in this study. We employed generalized interpolation material point (GIMP) method [7] with continuum surface tension (CSF) model [9] for surface tension and Perzyna model [24] for viscoelasto-plastic model, which will be described in Sects. 2.3 and 2.5, respectively. The interested reader about basics and formulation of MPM is referred to Sulsky et al. [30], Bardenhagen and

Kober [7] and Chen and Brannon [10] for a more detailed description of the standard MPM and GIMP.

2.1 Governing equations

The governing equations for fully coupled, transient thermo-mechanical problems in this study consist of three conservation laws and a viscoplastic constitutive relation. The conservation of mass, conservation of momentum and conservation of energy are written as follows, respectively,

$$\dot{\rho} + \rho \nabla \cdot \boldsymbol{v} = 0 \tag{1}$$

$$\rho \dot{\boldsymbol{v}} = \nabla \cdot \boldsymbol{\sigma} + \rho \boldsymbol{b} \tag{2}$$

$$\rho c \dot{T} = -\nabla \cdot \boldsymbol{q} + \rho s_{\text{laser}} + \rho l_s \dot{\xi}_s \tag{3}$$

where ρ is the density, $\boldsymbol{v}$ is the velocity, $\boldsymbol{\sigma}$ is the Cauchy stress, $\boldsymbol{b}$ is the body force per unit mass, c is the heat capacity, $\boldsymbol{q}$ is the heat flux, s_{laser} is the source term for the laser heating, l_s is the latent heat and ξ_s is volume fraction of solid. The superposed dot is the time derivative. The Fourier law of heat conduction, $\boldsymbol{q} = -\boldsymbol{k}\nabla T$, is employed. Thus, Eq. (3) can be rewritten as

$$\rho c \dot{T} = \nabla \cdot (\boldsymbol{k} \nabla T) + \rho s_{\text{laser}} + \rho l_s \dot{\xi}_s \tag{4}$$

where $\boldsymbol{k}$ is the thermal conductivity. s_{laser} and ξ_s, which are related to the thermal field, will be described in Sect. 2.4.

2.2 Discretization for momentum equation

In the standard MPM framework, the weak form of the momentum equation is used with a test function $\boldsymbol{w}$ as follows:

$$\int_\Omega \rho \boldsymbol{w} \cdot \dot{\boldsymbol{v}} \, \mathrm{d}\Omega = -\int_\Omega \rho \nabla \boldsymbol{w} \cdot \boldsymbol{\sigma}^s \, \mathrm{d}\Omega + \int_\Omega \rho \boldsymbol{w} \cdot \boldsymbol{b} \, \mathrm{d}\Omega + \int_S \boldsymbol{w} \cdot \bar{\boldsymbol{t}} \, \mathrm{d}S \tag{5}$$

where $\boldsymbol{\sigma}^s$ is the specific Cauchy stress tensor ($\boldsymbol{\sigma}^s = \boldsymbol{\sigma}/\rho$) and $\bar{\boldsymbol{t}}$ is the applied traction on the boundary S. The following approximation is introduced for density

$$\rho(\boldsymbol{x}, t) = \sum_{p=1}^{n_p} M_p \delta(\boldsymbol{x} - \boldsymbol{x}_p) \tag{6}$$

where $\delta(\boldsymbol{x})$ is the dirac delta function with dimension of the inverse of volume, $\boldsymbol{x}_p$ is the position of material point particle and n_p and M_p are the total number of material point particles used and the particle mass, respectively. Using Eq. (6), the following discrete form for the governing equation is obtained

$$\sum_p M_p \boldsymbol{w} \cdot \dot{\boldsymbol{v}} = -\sum_p M_p \nabla \boldsymbol{w} \cdot \boldsymbol{\sigma}^s + \sum_p M_p \boldsymbol{w} \cdot \boldsymbol{b} + \int_S \boldsymbol{w} \cdot \bar{\boldsymbol{t}} \, \mathrm{d}S. \tag{7}$$

Accordingly, the test function and its gradient are approximated as

$$\boldsymbol{w} = \sum_i \boldsymbol{w}_i N_i(\boldsymbol{x}) \tag{8}$$

$$\nabla \boldsymbol{w} = \sum_i \boldsymbol{w}_i \nabla N_i(\boldsymbol{x}) \tag{9}$$

where i is the node index. Substituting Eqs. (8) and (9) into Eq. (7) and using interpolation function N_i, the discrete governing equation for the conservation of momentum can be written as

$$m_i \boldsymbol{a}_i = \boldsymbol{f}_i^{\text{ext}} + \boldsymbol{f}_i^{\text{int}} + \boldsymbol{f}_i^{\text{sur}} \tag{10}$$

where $\boldsymbol{f}_i^{\text{int}}$ and $\boldsymbol{f}_i^{\text{ext}}$ are the internal and external load vectors, respectively, which are given by

$$\boldsymbol{f}_i^{\text{int}} = -\sum_{p=1}^{n_p} V_p \boldsymbol{\sigma}_p \cdot \nabla N_i \tag{11}$$

$$\boldsymbol{f}_i^{\text{ext}} = \sum_{p=1}^{n_p} M_p \boldsymbol{b} N_i + \int_S \bar{\boldsymbol{t}} N_i \, \mathrm{d}S, \tag{12}$$

and $\boldsymbol{f}_i^{\text{sur}}$ is the surface tension force. The formulation of $\boldsymbol{f}_i^{\text{sur}}$ will be presented in Sect. 2.3. For $N_i(\boldsymbol{x})$, we use the uniform GIMP (uGIMP) interpolation function presented in [7,28]. For time integrator, the explicit time stepping scheme is applied

$$\boldsymbol{a}_i^n = \frac{\boldsymbol{v}_i^{n+1} - \boldsymbol{v}_i^n}{\Delta t}. \tag{13}$$

Here, the velocity and position vector of material points are updated based on the time evolution scheme given as follows:

$$\boldsymbol{v}_p^{n+1} = \boldsymbol{v}_p^n + \Delta t \sum \frac{N_i(\boldsymbol{x}_p^n) \boldsymbol{f}_i^n}{m_i^n} \tag{14}$$

$$\boldsymbol{x}_p^{n+1} = \boldsymbol{x}_p^n + \Delta t \sum \frac{N_i(\boldsymbol{x}_p^n)(m\boldsymbol{v})_i^{n+1}}{m_i^n}. \tag{15}$$

Thereafter, the deformation gradient is updated using the relation $\dot{\boldsymbol{F}} = \boldsymbol{L}\boldsymbol{F}$,

$$\dot{\boldsymbol{F}}_p = \frac{\boldsymbol{F}_p^{n+1} - \boldsymbol{F}_p^n}{\Delta t} = \boldsymbol{L}_p^{n+1} \boldsymbol{F}_p^n \tag{16}$$

where $\boldsymbol{L}_p^{n+1} = \nabla \boldsymbol{v}_p^{n+1} = \sum \nabla N_i(\boldsymbol{x}_p)\boldsymbol{v}_i^{n+1}$ is the spatial velocity gradient. The deformation gradient at the next step is obtained as follows:

$$\boldsymbol{F}_p^{n+1} = (\boldsymbol{I} + \boldsymbol{L}_p^{n+1}\Delta t)\boldsymbol{F}_p^n \tag{17}$$

and the volume of each particle is updated by using the determinant of the deformation tensor

$$V_p^{n+1} = \det \boldsymbol{F}_p^{n+1} V_p^0 \tag{18}$$

where V_p^0 is the initial particle volume and V_p^{n+1} is the current particle volume. The stress analysis is described with a elastic–viscoplastic constitutive model in Sect. 2.5.

2.3 Formulation of surface tension

In order to describe the surface tension $\boldsymbol{f}_i^{\text{sur}}$, we mainly follow the methodology presented in Chen et al. [11] except the curvature. The curvature is computed using the level set function as in [37]. The surface tension force can be calculated as

$$\boldsymbol{f}_i^{\text{sur}} = V_c \gamma^{\text{sur}} \kappa_i \frac{\nabla m_i}{[m_i]} \frac{m_i}{< m_i >} \tag{19}$$

where V_c is the cell volume of background grid, γ^{sur} is the surface tension coefficient, κ_i is the curvature, $[m_i]$ is the density difference at the interface and $< m_i >$ is the average density of the interface. ∇m_i, the gradient of grid mass, is calculated by

$$\nabla m_i = \sum_{i'} \nabla N_{i'}(\boldsymbol{x}_i) m_{i'} \tag{20}$$

where $\sum_{i'}$ is a summation over the neighboring nodes of $\boldsymbol{x}_i$. For the curvature, the level set function is computed using following equation:

$$\phi(\boldsymbol{x}) = \min_p(\|\boldsymbol{x} - \boldsymbol{x}_p\| - r_p) \tag{21}$$

where $\boldsymbol{x}_p$ is the particle position and r_p is the particle radius. Then, $\phi(\boldsymbol{x}) = 0$ indicates the interface. We use the nine signed distances evaluated at a grid node and its neighbor nodes given by

$$\phi_n = \phi(\boldsymbol{x}_n) \tag{22}$$

where $\boldsymbol{x}_n \in \{\boldsymbol{x} | \boldsymbol{x}$ is the grid node $\}$ i and its neighbor node positions to solve least-squares problem to determine coefficients $a_0, a_1, \ldots, a_5$ of a local quadratic polynomial function $\tilde{\phi}_i(x, y)$ around the grid node i written by

$$\tilde{\phi}_i(x, y) = a_0 + a_1 x + a_2 y + a_3 x^2 + a_4 y^2 + a_5 xy. \tag{23}$$

Now, the first- and second-order derivatives of $\tilde{\phi}_i$ are readily computed. The curvature is obtained as follows:

$$\begin{aligned}\kappa_i &= \nabla \cdot \frac{\nabla \tilde{\phi}_i}{|\nabla \tilde{\phi}_i|}\bigg|_{(x,y)=(x_i,y_i)} \\ &= \frac{\tilde{\phi}_{i,xx}\tilde{\phi}_{i,y}^2 - 2\tilde{\phi}_{i,x}\tilde{\phi}_{i,y}\tilde{\phi}_{i,xy} + \tilde{\phi}_{i,yy}\tilde{\phi}_{i,x}^2}{(\tilde{\phi}_{i,x}^2 + \tilde{\phi}_{i,y}^2)^{3/2}}\bigg|_{(x,y)=(x_i,y_i)}\end{aligned} \tag{24}$$

where $\tilde{\phi}_{i,x} = \frac{\partial \tilde{\phi}_i}{\partial x}$, $\tilde{\phi}_{i,y} = \frac{\partial \tilde{\phi}_i}{\partial y}$, $\tilde{\phi}_{i,xx} = \frac{\partial^2 \tilde{\phi}_i}{\partial x^2}$, $\tilde{\phi}_{i,yy} = \frac{\partial^2 \tilde{\phi}_i}{\partial y^2}$, and $\tilde{\phi}_{i,xy} = \frac{\partial^2 \tilde{\phi}_i}{\partial x \partial y}$.

2.4 Thermal field and phase transition

In laser fusion AM process, phase transition has a crucial role in the overall process and the quality of the fabricated parts. In order to compute the temperature evolution, the weak form of the energy equation is used. Laser irradiation and latent heat are considered as heat source models and a heat flux-free condition is imposed at the natural boundary condition. The resulting equation is given as

$$\begin{aligned}\int_\Omega \rho w \cdot c\dot{T}\, \mathrm{d}\Omega = &\int_\Omega \rho \nabla w \cdot (\boldsymbol{k}\nabla T)\, \mathrm{d}\Omega + \int_\Omega \rho w \cdot s_{\text{laser}}\, \mathrm{d}\Omega \\ &+ \int_\Omega \rho w \cdot l_s \dot{\xi}_s\, \mathrm{d}\Omega.\end{aligned} \tag{25}$$

Then, the following discrete form for the governing equation is obtained using Eq. (6),

$$\begin{aligned}\sum_p M_p w \cdot c_p \dot{T} = &\sum_p M_p \nabla w \cdot \boldsymbol{k}\nabla T + \sum_p M_p w \cdot s_{\text{laser}} \\ &+ \sum_p M_p w \cdot l_s \dot{\xi}_s.\end{aligned} \tag{26}$$

As the interpolation function N_i and its gradient ∇N_i can be applied in the same manner as in Sect. 2.2, the MPM formulation for balance of energy is obtained as follows:

$$c_i \dot{T}_i = Q_i^{\text{int}} + Q_i^{\text{ext}} \tag{27}$$

where

$$c_i = \sum_{p=1}^{n_p} M_p c_p N_i(\boldsymbol{x}_p) \tag{28}$$

and

$$Q_i^{\text{int}} = \sum_p V_p(\boldsymbol{k}\nabla T) \cdot \nabla N_i \tag{29}$$

$$Q_i^{\text{ext}} = \sum_p M_p s_{\text{laser}} N_i + \sum_p M_p l_s \dot{\xi}_s N_i. \tag{30}$$

The thermal effects of the laser on the powder are computed using a laser heat source model with a Gaussian energy distribution [14]. The laser energy density in two dimensions is given by

$$s_{\text{laser}} = \frac{2AP}{\pi {r_0}^2 \eta_l} \exp\left(-2\frac{(x_l - x_p)^2}{r_0^2}\right) \cdot 0.6 \exp\left(\frac{y_l - y_p}{\eta_l}\right) \tag{31}$$

where A is the absorption coefficient, P is the input power, r_0 is the radius of laser spot, η_l is the penetration depth of laser and x_l and y_l are the laser positions. Again, x_p and y_p are the positions of material points.

In a system going through a phase transition via heat transfer, the total enthalpy H is represented by a sum of sensible heat h and latent heat ΔH,

$$H = h + \Delta H. \tag{32}$$

The latent heat is absorbed during melting process and released during crystallization process between T_c and T_m. We assume that the latent heat of fusion is equal to the latent heat of crystallization. The latent heat is given as $\Delta H = l_s \xi_s$.

To identify the volume fraction of solid phase ξ_s, a linear function is introduced [32],

$$\xi_s = 1 - \frac{(T - T_c)}{(T_m - T_c)} \tag{33}$$

where T_c and T_m are the crystallization and melting temperature of polymeric materials, respectively. The volume fractions of the solid and liquid phases satisfy $\xi_l + \xi_s = 1$. The specific heat c_p during the transition is interpolated using the fraction of phase as $c_p = \xi_s c_{ps} + \xi_l c_{pl}$.

2.5 Constitutive equation

A elasto-viscoplastic constitutive model is necessary in order to describe the behavior of melting and solidification in polymeric SLS process. As described in Sect. 1, polymeric powders are rapidly heated above T_m from around T_c and resolidification occurs due to the heat conduction, convection and radiation after the laser irradiation. The deformation with phase transition on the series of the process is irreversible. The physically based constitutive models have been proposed for viscoplastic behavior, e.g., [5]. On the other hand, the phenomenological-based constitutive models have been developed and sometimes provide an easier modeling approach. Perzyna's phenomenological formulation was supported by the thermodynamics of irreversible processes [24] and can be used to model the rate-dependent behavior of polymers, e.g., [2]. In our model, thus the Perzyna viscoplastic model incorporating a return mapping algorithm [27] is employed as a constitutive model.

The Eulerian infinitesimal strain rate $\dot{\boldsymbol{\epsilon}}$ is given by the spatial gradient of the deformation rate $\dot{\boldsymbol{u}}$ as

$$\dot{\boldsymbol{\epsilon}} = \{\text{grad}\, \dot{\boldsymbol{u}} + (\text{grad}\, \dot{\boldsymbol{u}})^T\}/2. \tag{34}$$

In order to describe the total strain rate of thermo-mechanical phenomena with phase change, the total strain rate $\dot{\boldsymbol{\epsilon}}$ is given by the sum of the elastic and plastic strain rates $\dot{\boldsymbol{\epsilon}}^e$ and $\dot{\boldsymbol{\epsilon}}^{pl}$, as well as the thermal strain rate $\dot{\boldsymbol{\epsilon}}^{\text{th}}$ and the transformation strain rate $\dot{\boldsymbol{\epsilon}}^m$ representing dilatation caused by phase change. This concept was introduced by Inoue and Wang [18].

$$\dot{\boldsymbol{\epsilon}} = \dot{\boldsymbol{\epsilon}}^e + \dot{\boldsymbol{\epsilon}}^{pl} + \dot{\boldsymbol{\epsilon}}^{\text{th}} + \dot{\boldsymbol{\epsilon}}^m. \tag{35}$$

The thermal strain rate $\dot{\boldsymbol{\epsilon}}^{\text{th}}$ is given by

$$\dot{\boldsymbol{\epsilon}}^{\text{th}} = \alpha \dot{T} \mathbf{1} \tag{36}$$

and the transformation strain rate $\dot{\boldsymbol{\epsilon}}^m$ due to solidification yields

$$\dot{\boldsymbol{\epsilon}}^m = \beta \dot{\xi}_s \mathbf{1} \tag{37}$$

where α and β denote the coefficients of thermal expansion and of dilatation due to solidification, respectively.

Thereafter, we compute an elastic trial stress and test for plastic loading. Trial stresses $\boldsymbol{\sigma}^{\text{trial}}$ and trial deviatoric stresses $\boldsymbol{s}^{\text{trial}}$ are given by

$$\boldsymbol{\sigma}_{n+1}^{\text{trial}} = p_{n+1}\mathbf{1} + \boldsymbol{s}_{n+1}^{\text{trial}} \tag{38}$$

$$\boldsymbol{s}_{n+1}^{\text{trial}} = 2\mu(\boldsymbol{\epsilon}_{n+1} - \boldsymbol{\epsilon}_n^{pl} - \boldsymbol{\epsilon}_n^{\text{th}} - \boldsymbol{\epsilon}_n^m) - \frac{1}{3}\text{tr}(\boldsymbol{\epsilon}_{n+1} - \boldsymbol{\epsilon}_n^{pl} - \boldsymbol{\epsilon}_n^{\text{th}} - \boldsymbol{\epsilon}_n^m)\mathbf{1} \tag{39}$$

where the pressure is given by $p_{n+1} = \lambda\, \text{tr}[\boldsymbol{\epsilon}_{n+1}]$. We then plug trial deviatoric stress in the yield function given by

$$f_{n+1}^{\text{trial}} := \|\boldsymbol{s}_{n+1}^{\text{trial}}\| - \sqrt{\frac{2}{3}}[\sigma_Y + H\alpha_n^{pl}] \tag{40}$$

where σ_Y is the yielding stress, H is the hardening coefficient and α^{pl} is the equivalent plastic strain. When f^{trial} is a non-negative, a plastic step starts and the consistency parameter $\Delta\gamma$ is obtained in the following equation:

$$\Delta\gamma = \frac{f_{n+1}^{\text{trial}}/2\mu}{\tau/\Delta t + 1 + H/3\mu} \quad \text{where}$$
$$\tau := \frac{\eta}{2\mu} \quad \text{(the relaxation time)} \tag{41}$$

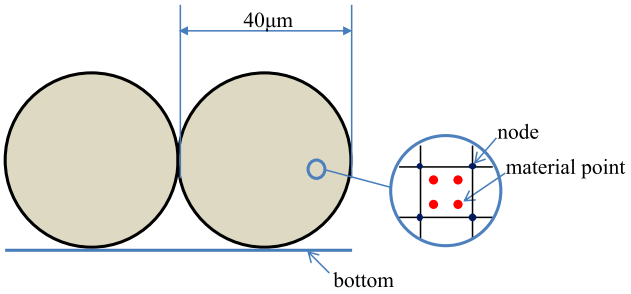

Fig. 2 Schematic illustration of the model in this study

where η is the viscosity. The variables λ and μ are the Lame's constants. Afterward, $\boldsymbol{\epsilon}^{pl}$, α^{pl}, $\boldsymbol{s}$ and $\boldsymbol{\sigma}$ are updated in plastic step as follows, respectively.

$$\boldsymbol{\epsilon}^{pl}_{n+1} = \boldsymbol{\epsilon}^{pl}_{n} + \Delta\gamma \boldsymbol{n}^{\text{trial}} \quad \text{with} \quad \boldsymbol{n}^{\text{trial}} = \frac{\boldsymbol{s}^{\text{trial}}}{\|\boldsymbol{s}^{\text{trial}}\|} \tag{42}$$

$$\alpha^{pl}_{n+1} = \alpha^{pl}_{n} + \sqrt{\frac{2}{3}}\Delta\gamma \tag{43}$$

$$\boldsymbol{\sigma}_{n+1} = p_{n+1}\,\mathbf{1} + \boldsymbol{s}_{n+1} \tag{44}$$

$$\boldsymbol{s}_{n+1} = 2\mu\,\text{dev}[\boldsymbol{\epsilon}_{n+1} - \boldsymbol{\epsilon}^{pl}_{n+1} - \boldsymbol{\epsilon}^{\text{th}}_{n+1} - \boldsymbol{\epsilon}^{m}_{n+1}]. \tag{45}$$

Finally, $\boldsymbol{\sigma}$ is substituted for the stress in Eq. (11) to obtain internal force $\boldsymbol{f}^{\text{int}}_i$ in MPM framework.

3 Results and discussion

In order to validate the proposed method, a simple numerical test case is examined in this section. First, the simulation conditions such as initial set up, laser conditions and material parameters are introduced. Following this, the consolidation behavior of powders during SLS process is investigated under systematic laser conditions.

3.1 Simulation conditions and material data

The geometry for the test case is illustrated in Fig. 2. The geometrical setup consists of two powder particles with 40 μm in diameter. The top surface of the material and both side walls are insulated, and the bottom temperature is kept at a constant temperature for preheating. The gradient of grid mass, ∇m_i which is required for surface tension is obtained by using the neighboring nodes as shown in Eq. (20). Since the powder touches the wall and bottom at the initial geometry, an extra cell is added to left and right walls and the bottom to consider the accurate surface tension. These cells are only used for calculating the surface tension. Polyamide 12 is considered for the test case simulations since it is used most often in SLS process. Two types of spatial discretization are prepared as shown in Table 1. The grid spacing is 2 μm or 4 μm, and four material points are set per one cell.

Table 1 Spatial discretization

	Grid space (μm)	Nodes	Material points
Fine	2	1163	2578
Coarse	4	322	632

Table 2 Laser conditions

Laser parameter	Notation	Value
Laser power	P	5, 15, 25 W
Laser radius	r_0	30, 50, 70 μm
Laser velocity	v_{laser}	0 or 4 m/s
Absorptivity	A	0.85%
Penetration depth	η_l	100 μm

The laser power and radius are systematically varied to evaluate melting behavior of particle pairs as shown in Table 2. The laser scanning condition is also applied. The material parameters used in the simulations are shown in Table 3. The viscosity η of PA12 has been taken from Zhao et al. [38]. The viscosity that depends on the temperature is modeled using the experimental values. We use the experimental surface tension coefficient γ^{sur} obtained by Zhao et al. [38]. Young's modulus in the liquid phase has been chosen from the general crystalline polymer values [15]. In the solid phase, the modulus is a function of temperature. The starting temperature in the SLS is just below T_c; thus, the modulus of the solid phase has been chosen an order of magnitude larger than that of liquid phase.

For the calculation of the time step size, the restriction is considered for the standard advective CFL condition,

$$\Delta t_c \leq h\sqrt{\frac{\rho}{E}} \tag{46}$$

and for the surface tension [9],

$$\Delta t_{\text{surf}} \leq \sqrt{\frac{\rho h^3}{\gamma^{\text{surf}}}} \tag{47}$$

and for the thermal field

$$\Delta t_T \leq \frac{h^2 \rho c}{4k} \tag{48}$$

where h is the grid spacing. In case of a fine discretization (Table 1), the sufficiently small time step of $\Delta t = 5 \times 10^{-8}$ s is used.

Table 3 Material parameters

Thermo-mechanical parameter	Notation	Value
Heat conductivity	k_m	0.24 W/m °C
	k_c	0.28 W/m °C
Specific heat	c_m	2700 J/kg °C
	c_c	2700 J/kg °C
Latent heat	l_s	50 kJ/kg
Melting temperature	T_m	175°C
Crystallization temperature	T_c	146°C
Density	ρ	1020 kg/m^3
Thermal expansion coefficient	α	15×10^{-5}/K ($T \leq T_c$)
		5×10^{-5}/K ($T \geq T_m$)
Dilatation of solidification	β	1.5%
Poisson's ratio	ν	0.42
Young's modulus	E	1×10^5 Pa ($T \leq T_c$)
		1×10^4 Pa ($T \geq T_m$)
Viscosity	η	1,30,219 $\times \exp(-0.02 \times T)$ Pa s
Surface tension coefficient	γ^{sur}	36.3×10^{-3} N/m
Yield stress	σ^y	1×10^5 Pa ($T \leq T_c$)
		1×10^4 Pa ($T \geq T_m$)
Hardening coefficient	H	1×10^5 Pa ($T \leq T_c$)
		0 Pa ($T \geq T_m$)
Baseplate temperature	T_B	140°C

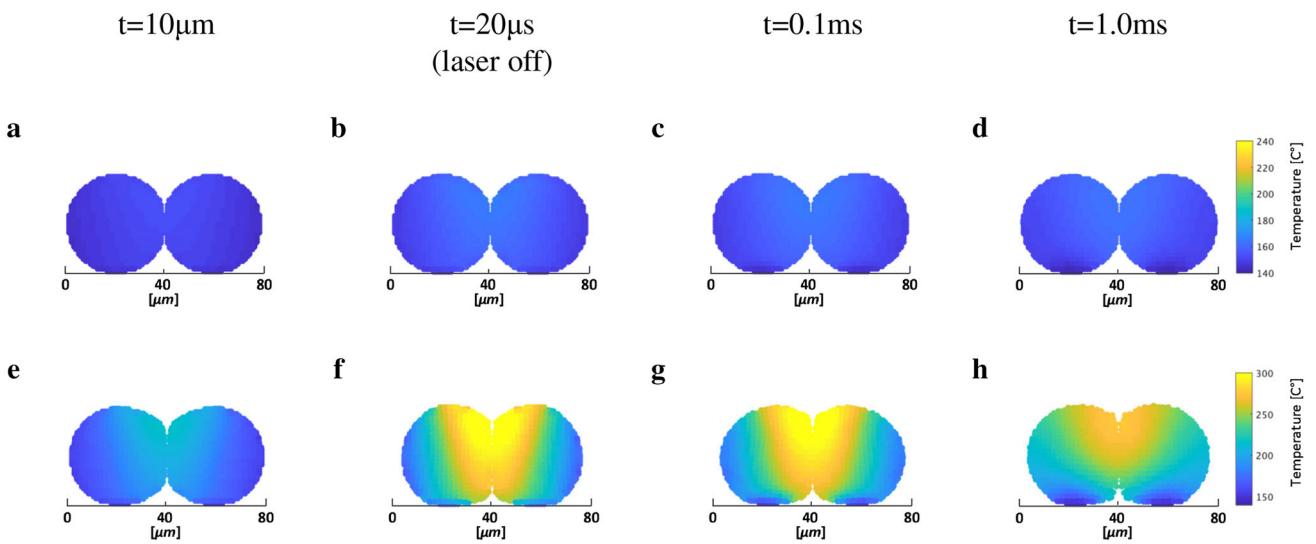

Fig. 3 Evolution of temperature and deformation as a function of laser power; **a**–**d** laser power is 5 W, **e**–**h** laser power is 25 W

3.2 Particle fusion analysis

Figure 3 shows the comparison of laser power on the evolution of temperature and deformation of powder particles using the fine spatial discretization. There is no notable change in the deformation of the particles at the laser power of 5 W. In contrast, neck growth occurs and particles are consolidated at the laser power of 25 W. In order to evaluate the consolidation behavior, the neck length was measured using the level set function ϕ used for tracking the interface as shown in Fig. 4. The neck length is defined as a contact line L, starting from the neck length of 8 µm, as shown in Fig. 4a. When a coarse spatial discretization (Table 1) is applied, the contact line is hardly changed regardless of laser power, radius. Accordingly, the fine spatial discretization was adopted in the analysis. Figure 5 summarizes the con-

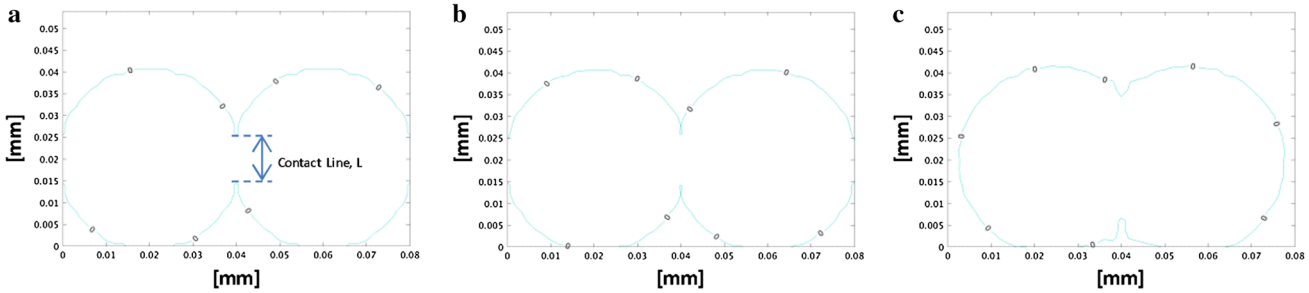

Fig. 4 Evaluation for consolidation using level set function ϕ; **a** initial state, **b** $P = 5$ W, time $= 1$ ms, **c** $P = 25$ W, time $= 1$ ms

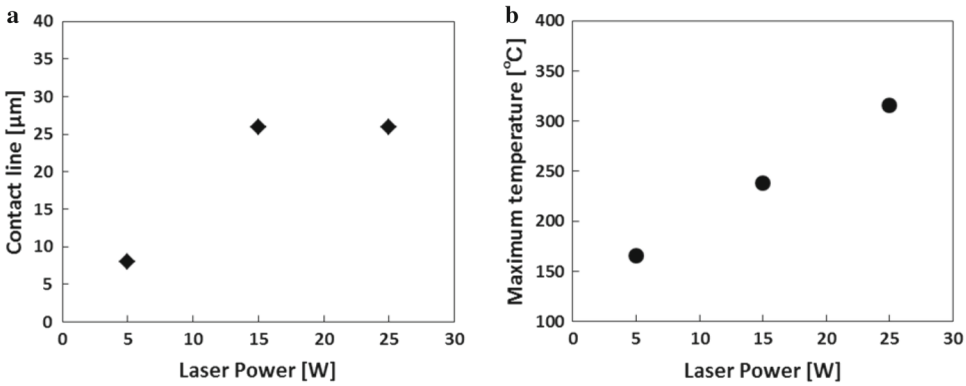

Fig. 5 Contact line and maximum temperature as a function of laser power. **a** Contact line of particle pair at the 1 ms. **b** Maximum temperatures during the process. The laser power is 15 W

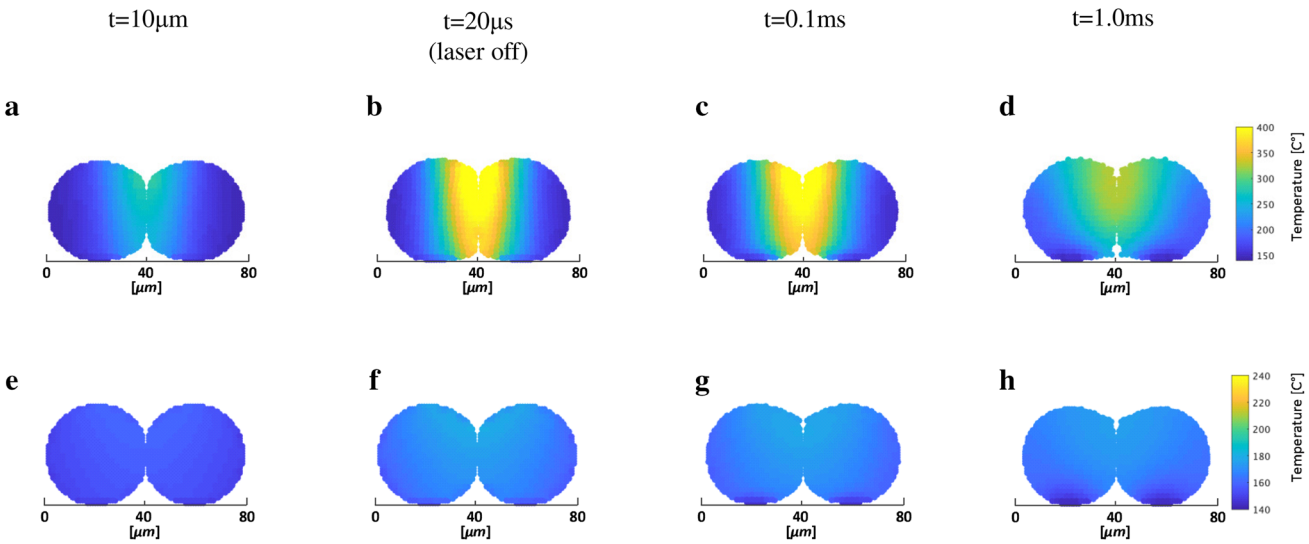

Fig. 6 Evolution of temperature and deformation as a function of laser radius; **a**–**d** laser radius is 30 μm; **e**–**h** laser radius is 70 μm. The laser power is 15 W

tact line and maximum temperature as a function of laser power. When the laser power is small, the contact line does not change, while when the laser power is sufficiently large, the neck grows and the powders are consolidated. From the result of the overall temperature distribution (Fig. 3) and the maximum temperature (Fig. 5b), laser power of certain level or more is required for consolidation under the driving force of surface tension. This idea can be further understood by the following results of the influence of the laser radius. Figure 6 shows the comparison of laser radius on the evolution of temperature and deformation of powder particles, and Fig. 8a, b summarizes the contact line and maximum temperature as a function of laser radius. The laser with large radius heats up the whole particle pairs, and the neck grows with the maximum temperature well above the T_m. Reducing the laser radius causes the maximum temperature to rise, resulting in neck growth. Figure 7 shows the consolidation evolution with moving laser at a laser power of 15 W and a

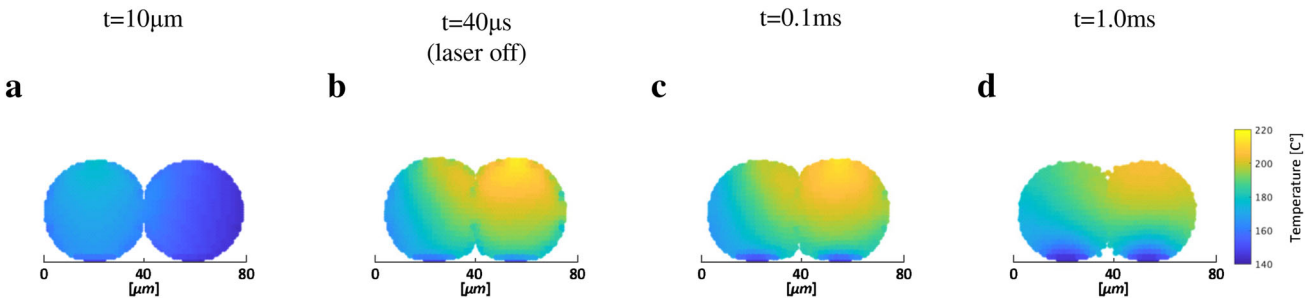

Fig. 7 Consolidation evolution with moving laser at a laser power of 15 W and a laser radius of 50 μm. Scanning speed is 4 m/s. The laser starts at the left edge and ends at the right edge of the powder pairs

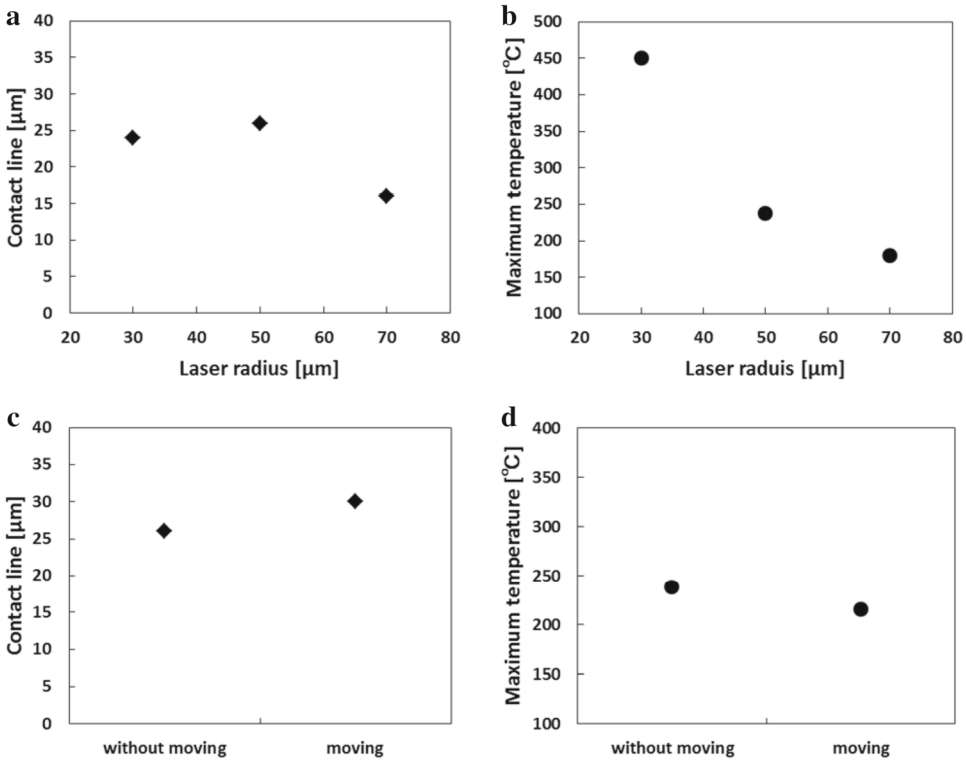

Fig. 8 Contact line and maximum temperature as a function of laser radius and with/without moving laser. **a**, **c** Contact line of particle pair at the 1 ms. **b**, **d** Maximum temperatures during the process. The laser power is 15 W

laser radius of 50 μm. The temperature gradient is reduced because of laser scanning. The temperature increase becomes line asymmetric with respect to the contact line of particles at the initial state. As a result, the powders slide slightly to the left because the effect of surface tension is asymmetric. The consolidation proceeds in the laser scanning condition than in non-scanning condition. The scanning reduces the overall temperature gradient and maximum temperature in spite of the longer irradiation time (Figs. 7, 8c, d).

Different melting and consolidation behavior due to the laser conditions are confirmed in the constructed model. Melting and consolidation of two particles during SLS are basic nature in determining the final product quality. Incomplete consolidation (e.g., Fig. 3a–d) results in poor mechanical properties; thus, the screening methods using the numerical model are effective. The model can help to screen the laser conditions in the consolidation of two particles, melted by a laser.

4 Conclusions

In summary, a novel MPM framework for SLS process is developed using continuum surface force model and Perzyna-type viscoelasto-plastic model associated with a thermal field and phase transitions. Laser melting phenomena are introduced, and the consolidation of material is observed at the powder particle scale. The model can help to evaluate the different consolidation behaviors of particles due to variations in laser conditions and provide the guideline to control them. The proposed MPM model in our work uses the explicit scheme for time integrator whose time step size

must satisfy CFL condition for stability. An implicit formulation could be used to address the stability issue in future work. Although MPM has high computational cost, like other particle-based methods, the proposed MPM framework has a potential to perform a sophisticated melting and consolidation simulation of SLS at industrial scales by using a GPU parallel computing.

Compliance with ethical standards

Conflict of interest The authors declare that there is no conflict of interest of any type during the production of this research.

References

1. Abdul-Hameed H, Messager T, Ayoub G, Zaïri F, Naït-Abdelaziz M, Qu Z, Zaïri F (2014) A two-phase hyperelastic-viscoplastic constitutive model for semi-crystalline polymers: application to polyethylene materials with a variable range of crystal fractions. J Mech Behav Biomed Mater 37:323–332. https://doi.org/10.1016/j.jmbbm.2014.04.016
2. Abu Al-Rub R, Tehrani A, Darabi M (2015) Application of a large deformation nonlinear-viscoelastic viscoplastic viscodamage constitutive model to polymers and their composites. Int J Damage Mech 24:198–244. https://doi.org/10.1177/1056789514527020
3. Aleksy N, Kermuche G, Vautrin A, Bergheau JM (2010) Numerical study of scratch velocity effect on recovery of viscoelastic-viscopkastic solides. Int J Mech Sci 52:455–463
4. Ammer R, Markl M, Ljungblad U, Körner C, Rüde U (2014) Simulating fast electron beam melting with a parallel thermal free surface lattice boltzmann method. Comput Math Appl 67(2):318–330. https://doi.org/10.1016/j.camwa.2013.10.001 Mesoscopic Methods for Engineering and Science (Proceedings of ICMMES-2012, Taipei, Taiwan, 23–27 July 2012)
5. Arruda EM, Boyce MC, Jayachandran R (1995) Effects of strain rate, temperature and thermomechanical coupling on the finite strain deformation of glassy polymers. Mech Mater 19(2):193–212. https://doi.org/10.1016/0167-6636(94)00034-E
6. Balemans C, Jaensson N, Hulsen M, Anderson P (2018) Temperature-dependent sintering of two viscous particles. Add Manuf 24:528–542. https://doi.org/10.1016/j.addma.2018.09.005
7. Bardenhagen SG, Kober EM (2004) The generalized interpolation material point method. Comput Model Eng Sci 5(6):477–496. https://doi.org/10.3970/cmes.2004.005.477
8. Bierwisch C, Mohseni-mofidi S, Dietemann B, Rudloff J, Baumann S, Popp K, Lang M (2019) Particle-based simulations and dimensional analysis of selective laser sintering of PA12 powder. In: Auricchio F, Rank E, Steinmann P, Kollmannsberger S, Morganti S (eds) Sim-AM 2019. CIMNE, Barcelona, pp 316–327
9. Brackbill J, Kothe D, Zemach C (1992) A continuum method for modeling surface tension. J Comput Phys 100(2):335–354. https://doi.org/10.1016/0021-9991(92)90240-Y
10. Chen Z, Brannon RM (2002) An evaluation of the material point method. SAND report SAND2002-0482
11. Chen L, Lee J, Chen Cf (2012) On the modeling of surface tension and its applications by the generalized interpolation material point method. Comput Model Eng Sci 86:199–224. https://doi.org/10.3970/cmes.2012.086.199
12. Dong Y, Grabe J (2018) Large scale parallelisation of the material point method with multiple GPUS. Comput Geotech 101:149–158. https://doi.org/10.1016/j.compgeo.2018.04.001
13. Drozdov A, Christiansen J (2003) Model for the viscoelastic and viscoplastic responses of semicrystalline polymers. J Appl Polym Sci 88:1438–1450. https://doi.org/10.1002/app.11797
14. Du Y, You X, Qiao F, Guo L, Liu Z (2019) A model for predicting the temperature field during selective laser melting. Results Phys 12:52–60. https://doi.org/10.1016/j.rinp.2018.11.031
15. Fincan M (2015) Assessing viscoelastic properties of polydimethylsibxane (PDMS) using loading and unloading of the macroscopic compression test. PhD thesis, University of South Florida
16. Fürstenau JP, Wessels H, Weißenfels C, Wriggers P (2020) Generating virtual process maps of SLM using powder scale SPH simulations. Comput Part Mech 7:655–677. https://doi.org/10.1007/s40571-019-00296-3
17. Ganeriwala R, Zohdi T (2016) A coupled discrete element-finite difference model of selective laser sintering. Granul Matter 18:21. https://doi.org/10.1007/s10035-016-0626-0
18. Inoue T, Wang ZG (1988) Thermal and mechanical fields in continuous casting slab—a steady state analysis incorporating solidification. Arch Appl Mech 58(4):265–275. https://doi.org/10.1007/BF00535936
19. Kermouche G, Aleksy N, Bergheau JM (2013) Viscoelastic-viscoplastic modelling of the scratch response of PMMA. Adv Mater Sci Eng. https://doi.org/10.1155/2013/289698
20. Khairallah SA, Anderson AT, Rubenchik A, King WE (2016) Laser powder-bed fusion additive manufacturing: physics of complex melt flow and formation mechanisms of pores, spatter, and denudation zones. Acta Mater 108:36–45. https://doi.org/10.1016/j.actamat.2016.02.014
21. Kinstlinger IS, Bastian AA, Paulsen SJ, Hwang DH, Ta AH, Yalacki DR, Schmidt T, Miller JS (2016) Open-source selective laser sintering (opensls) of nylon and biocompatible polycaprolactone. PLoS One 11:e0147399
22. Kruth JP, Levy G, Schindel R, Craeghs T, Yasa E (2008) Consolidation of polymer powders by selective laser sintering. In: Proceedings of the 3rd international conference on polymers and moulds innovations, pp 15–30
23. Majewski C, Zarringhalam H, Hopkinson N (2008) Effect of the degree of particle melt on mechanical properties in selective laser-sintered Nylon-12 parts. Proc Inst Mech Eng, Part B: J Eng Manuf 222:1055–1064. https://doi.org/10.1243/09544054JEM1122
24. Perzyna P (1971) Thermodynamic theory of viscoplasticity. Adv Appl Mech 11:313–354
25. Peyre P, Rouchausse Y, Defauchy D, Regnier G (2015) Experimental and numerical analysis of the selective laser sintering (SLS) of PA12 and PEKK semi-crystalline polymers. J Mater Process Technol 225:326–336. https://doi.org/10.1016/j.jmatprotec.2015.04.030
26. Russell M, Souto-Iglesias A, Zohdi T (2018) Numerical simulation of laser fusion additive manufacturing processes using the SPH method. Comput Methods Appl Mech Eng 341:163–187. https://doi.org/10.1016/j.cma.2018.06.033
27. Simo JC, Hughes TJR (1998) Computational inelasticity. Springer, New York
28. Steffen M, Wallstedt P, Guilkey J, Kirby R, Berzins M (2008) Examination and analysis of implementation choices within the material point method (MPM). Comput Model Eng Sci 31(2):107–127
29. Stomakhin A, Schroeder C, Jiang C, Chai L, Teran J, Selle A (2014) Augmented MPM for phase-change and varied materials. ACM Trans Graph 33(4):1–11. https://doi.org/10.1145/2601097.2601176

30. Sulsky D, Chen Z, Schreyer H (1994) A particle method for history-dependent materials. Comput Methods Appl Mech Eng 118(1):179–196. https://doi.org/10.1016/0045-7825(94)90112-0
31. Sulsky D, Zhou SJ, Schreyer HL (1995) Application of a particle-in-cell method to solid mechanics. Comput Phys Commun 87(1–2):236–252. https://doi.org/10.1016/0010-4655(94)00170-7
32. Voller V, Swaminathan C (1991) General source-based method for solidification phase change. Numer Heat Trans, Part B: Fundam 19(2):175–189. https://doi.org/10.1080/10407799108944962
33. Wang X, Qiu Y, Slattery SR, Fang Y, Li M, Zhu SC, Zhu Y, Tang M, Manocha D, Jiang C (2020) A massively parallel and scalable multi-cpu material point method. ACM Trans Graph 39(4). https://doi.org/10.1145/3386569.3392442
34. Wessels H, Weißenfels C, Wriggers P (2018) Metal particle fusion analysis for additive manufacturing using the stabilized optimal transportation meshfree method. Comput Methods Appl Mech Eng 339:91–114. https://doi.org/10.1016/j.cma.2018.04.042
35. Yan W, Ge W, Qian Y, Lin S, Zhou B, Liu WK, Lin F, Wagner GJ (2017) Multi-physics modeling of single/multiple-track defect mechanisms in electron beam selective melting. Acta Mater 134:324–333. https://doi.org/10.1016/j.actamat.2017.05.061
36. Yang WC, Arduino P, Miller GR, Mackenzie-Helnwein P (2018) Smoothing algorithm for stabilization of the material point method for fluid solid interaction problems. Comput Methods Appl Mech Eng 342:177–199. https://doi.org/10.1016/j.cma.2018.04.041
37. Zhang F, Zhang X, Sze KY, Lian Y, Liu Y (2017) Incompressible material point method for free surface flow. J Comput Phys 330:92–110
38. Zhao M, Drummer D, Wudy K, Drexler M (2015) Sintering study of polyamide 12 particles for selective laser melting. Int J Recent Contrib Eng Sci IT 3:28–33